Study of Time-Resolved Vortex Structure of In-Cylinder Engine Flow Fields Using Proper Orthogonal Decomposition Technique

Hanyang Zhuang
University of Michigan – Shanghai Jiao Tong University Joint Institute,
Shanghai Jiao Tong University,
800 Dongchuan Rd.,
Shanghai 200240, China
e-mail: zhuanghany11@sjtu.edu.cn

David L.S. Hung
Mem. ASME
University of Michigan – Shanghai Jiao Tong University Joint Institute,
Shanghai Jiao Tong University,
800 Dongchuan Rd.,
Shanghai 200240, China
e-mail: dhung@sjtu.edu.cn

Hao Chen
Department of Mechanical Engineering,
The University of Michigan,
2026 W. E. Lay Automotive Laboratory,
1231 Beal Avenue,
Ann Arbor, MI 48109-2133
e-mail: haochen@umich.edu

The structure of in-cylinder flow field makes significant impacts on the processes of fuel injection, air–fuel interactions, and flame development in internal combustion engines. In this study, the implementation of time-resolved particle image velocimetry (PIV) in an optical engine is presented. Flow field PIV images at different crank angles have been taken using a high-speed double-pulsed laser and a high-speed camera with seeding particles mixed with the intake air. This study is focused on measuring the flow fields on the swirl plane at 30 mm below the injector tip under various intake air swirl ratios. A simple algorithm is developed to identify the vortex structure and to track the location and motion of vortex center at different crank angles. Proper orthogonal decomposition (POD) has been used to extract the ensemble and variation information of the vortex structure. Experimental results reveal that strong cycle-to-cycle variations exist in almost all test conditions. The vortex center is difficult to identify since multiple, but small scale, vortices exist during the early stage of the intake stroke. However, during the compression stroke when only one vortex center exists in most cycles, the motion of vortex center is found to be quite similar at different intake swirl ratios and engine speeds. This is due to the dominant driving force exerted by the piston's upward motion on the in-cylinder air. [DOI: 10.1115/1.4029600]

Introduction

Novel powertrain technologies have allowed automobiles to improve engine power and performance. For example, vehicles with spark-ignition direct-injection (SIDI) engines show remarkable advantages in lower fuel consumptions, better air–fuel ratio control, and reduced emissions. However, as the legislations become stricter on particulate matter emission, further improvements of in-cylinder mixing processes in SIDI engines are needed.

With the accessibility of optical engines and high-speed laser diagnostics, researchers are able to visualize the processes taking place in an engine cylinder with higher temporal and spatial resolutions. Sick et al. [1,2] reviewed the latest high-speed imaging applications in SIDI engines. They concluded that the intake air flow fields make the most significant impacts among all the in-cylinder processes since air flow in the cylinder affects the spray structure, air–fuel mixing, and flame propagation.

Extensive research has also been made using PIV to study the in-cylinder flow field structures. Flow fields can be normally visualized from two spatial directions: (1) swirl plane in which the flow rotates in the plane parallel to the piston top; and (2) tumble plane in which the flow is perpendicular to the piston top. The air flow motion in both directions also influences other in-cylinder processes such as fuel–air mixture formation and flame initiation. Since the in-cylinder air motion creates strong vortices, the vortex center identification algorithms have also been developed [3]. Other researchers analyzed the tumble and swirl plane PIV measurements along with the vortex center information extracted at various crank angles in optical engines [4,5]. They found larger cycle-to-cycle variations of flow fields during intake stroke while only small variations were present during compression stroke. In addition, POD has been introduced to flow field for the analysis of cycle-to-cycle fluctuations. The applications of POD in flow field analysis using PIV, and the misfire analysis using PIV and planar laser induced fluorescence were done by Chen et al. [6,7]. In addition, combining the PIV, POD, and vortex identification had also been implemented to analyze the flow field and its fluctuation in a circular duct, and both turbulent fluctuations and unsteady swirl motions were observed [8]. Moreover, applying the phase-invariant POD method to analyze the time-resolved swirl plane PIV flow fields in an optical diesel engine was also attempted to provide an evolutionary study of the flow field as a function of engine crank angle degree [9].

In this study, the in-cylinder air flow and vortex structures of various crank angles are investigated. The intake air flow fields of 200 consecutive cycles are recorded in an optical engine using high-speed PIV with a resolution of 10 crank angle interval between each set of PIV images, starting from early intake stroke to late compression stroke. POD is applied to determine the ensemble average and variations of the flow field structure among all cycles. Afterward, the first few modes of POD are extracted to identify the structure change and variations of vortex center and vortex core. The organization of this paper is as follows: an Experimental Setup section is first discussed, followed by Data Processing Techniques section including "POD" section and the algorithms for identifying the vortex center and vortex core. The analysis and results of the PIV and vortex information are discussed, and finally, a "Summary" section of this study is provided.

Contributed by the Turbomachinery Committee of ASME for publication in the Journal of Engineering for Gas Turbines and Power. Manuscript received December 8, 2014; final manuscript received January 7, 2015; published online February 10, 2015. Editor: David Wisler.

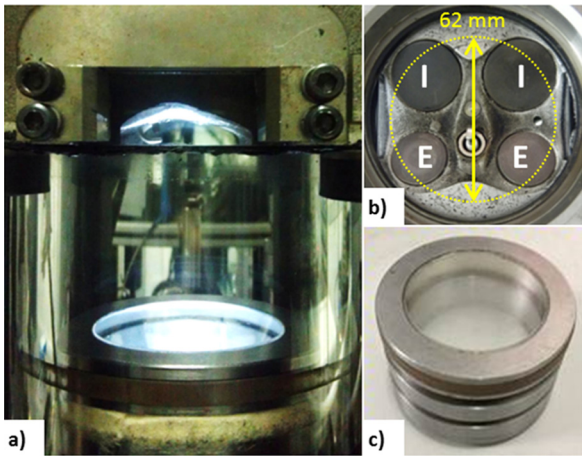

Fig. 1 (*a*) Optical liner and pent-roof window; (*b*) cylinder head and valve arrangement (dotted circle shows the visible area); and (*c*) quartz optical piston

Experimental Setup

Figure 1 depicts the optical engine in this study with various optical components and cylinder head configuration. The optical liner provided a direct access to steer a laser sheet into the cylinder. The quartz inserted optical piston was used for high-speed camera to record the images inside the engine along a swirl plane.

The PIV test was implemented by adding fine silicon oil droplets to the intake air. The oil droplets were generated by a TSI 6-jet atomizer. A high-speed double-pulsed Nd:YLF laser (Litron LDY300 PIV) with a wavelength of 527 nm was used as the light source to illuminate the oil droplets in the air. To illuminate the whole focal plane, a set of optics was used to convert the laser beam into a laser sheet with a thickness of 1 mm. A high-speed camera (Phantom V7.3) was set up to record the images of the moving oil droplets through a 45 deg mirror located centrally below the optical piston.

The schematic of the experimental setup is depicted in Fig. 2. The focal plane was positioned at 30 mm below the injector tip since it was a representative plane for both the spray formation and intake air flow field. The optical engine was motored using an AVL dyno at 1300 rpm with variable intake swirl ratio which was achieved by setting the angle of a swirl valve mounted in one of the two intake runners. The intake air with high swirl ratio (5.68) was achieved by completely shutting off the swirl valve to create a strong intake swirl motion. Both flow field and vortex structure were studied in this investigation for a high intake air swirl ratio.

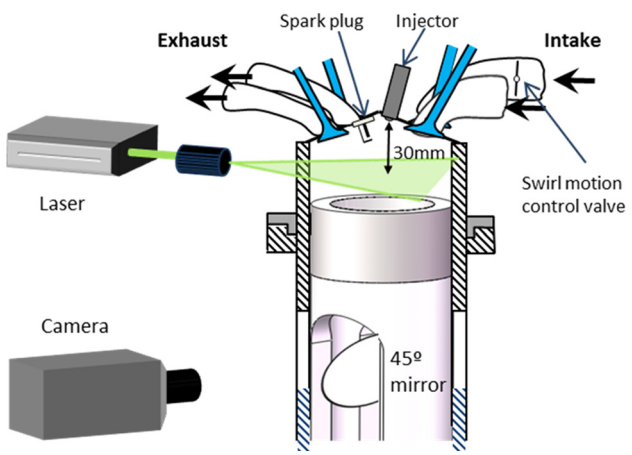

Fig. 2 Schematic of the experimental setup

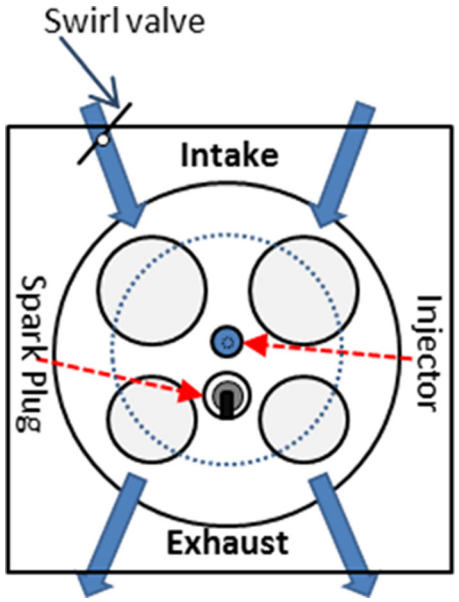

Fig. 3 Schematic of cylinder head with the same orientation of the following PIV images

Due to the limitation of laser energy attenuation with increasing frequency, a recording frequency at 780 Hz was compromised to fulfill the requirement of taking images at each 10 crank angle degree (CAD) from −300 CAD after top dead center (ATDC) to −60 CAD ATDC. When the piston was at a crank angle of earlier than −300 CAD ATDC and later than −60 CAD ATDC, the laser sheet was blocked by the piston. Therefore, the recording duration was limited by the location of the focal plane selected.

In addition to the cross section schematic of the whole experimental setup, Fig. 3 depicts the view of the cylinder head which was in the same orientation of the PIV images in the Results and Analysis section to be discussed later. The intake valves were located on the top of the circular viewable area while the exhaust valves were at the bottom. The upper left intake port was blocked by closing the swirl motion control valve to create a high intake swirl flow in clockwise direction.

Data Processing Techniques

In this section, the data processing techniques with detail information of the POD and vortex structure identification are discussed. Complementary information of POD analysis can be found in Ref. [10]. The identification of vortex center and vortex core is discussed in Ref. [8].

POD. POD is a statistical method to decompose a set of correlated target vectors into a set of linear independent bases and corresponding coefficients. The bases, which are called POD modes below, have the property such that the first mode captures the most significant characteristics of the input dataset, and the higher modes illustrate the less significant information. This technique can be applied to both scalar field such as the light scattering intensity of the spray images, the flame luminance of the combustion images, and vectors of the velocity flow field. In this section only, the basic principle of POD is presented while a more detailed introduction and guidance to POD including a code of MATLAB can be found in aforementioned complementary information [10].

Suppose that a set of scalar fields is obtained by high-speed imaging which are called the snapshots, as indicated by a matrix $s^{(k)}_{(i,j)}$. The index $k = 1, 2, \ldots, K$ means that there are totally K

scalar fields while i and j are the grid sizes of the corresponding scalar fields, i.e., the row and column pixels of the image. A set of spatial bases or POD modes (that is, a matrix defined as $\boldsymbol{\varphi}_{m(i,j)}, m = 1, 2, \ldots M$ and with the same size of the snapshot matrix) can be obtained after the decomposition process with the corresponding coefficients $c_m^{(k)}$ (a scalar indicating the coefficient of mth mode to the kth snapshot). The modes are orthonormal, meaning that they are orthogonal to each other, and the magnitude of each mode is equal to unity. The number of modes can only be less than or equal to the number of snapshots. However, for typical applications, the number of modes and snapshots are identical. The following equation shows the expression of the snapshots to be reconstructed by the modes and coefficients:

$$\boldsymbol{s}^{(k)} = \sum_{m=1}^{M} c_m^{(k)} \boldsymbol{\varphi}_m \tag{1}$$

The process to obtain the modes and coefficients is stated as follows: for the given K images with the same size $I \times J$, the first step is to reshape the $I \times J$ matrix into a row vector with dimension $1 \times (I \times J)$. Then, a $K \times (I \times J)$ snapshot matrix $\boldsymbol{R}$ can be regrouped by collecting all row vectors together, as follows:

$$\boldsymbol{R} = \begin{bmatrix} s_{i=1,j=1}^{(1)} & s_{i=1,j=2}^{(1)} & \cdots & s_{i=1,j=J}^{(1)} & s_{i=2,j=1}^{(1)} & \cdots & s_{i=I,j=J}^{(1)} \\ s_{i=1,j=1}^{(2)} & s_{i=1,j=2}^{(2)} & \cdots & s_{i=1,j=J}^{(2)} & s_{i=2,j=1}^{(2)} & \cdots & s_{i=I,j=J}^{(2)} \\ \vdots & \vdots & \vdots & \vdots & \vdots & \vdots & \vdots \\ s_{i=1,j=1}^{(K)} & s_{i=1,j=2}^{(K)} & \cdots & s_{i=1,j=J}^{(K)} & s_{i=2,j=1}^{(K)} & \cdots & s_{i=I,j=J}^{(K)} \end{bmatrix} \tag{2}$$

Afterward, the corresponding spatial correlation matrix $\boldsymbol{C}$ of the scalar field matrix $\boldsymbol{R}$ is defined as

$$\boldsymbol{C} = \frac{1}{K} \boldsymbol{R}\boldsymbol{R}^{\mathrm{T}} \tag{3}$$

The property of POD modes which captures the most dominant structure of the snapshots is expressed by satisfying the following equation:

$$\sum_{k=1}^{K} \left\| \boldsymbol{s}^{(k)} - \sum_{m=1}^{N} c_m^{(k)} \boldsymbol{\varphi}_m \right\|^2 \rightarrow \min \tag{4}$$

where $\| \cdot \|$ denotes the L^2 norm. The value noted by N in the summation operator is any arbitrary integer from 1 to M, which indicates that for any linear combinations of the first N POD modes and their coefficients, Eq. (1) is satisfied. This property is realized by solving the eigenvalue problem of the correlation matrix $\boldsymbol{C}$.

$$\boldsymbol{C}\boldsymbol{\beta}_m = \lambda_m \boldsymbol{\beta}_m \tag{5}$$

Using singular value decomposition, a decreasing order of the eigenvalues $(\lambda_m, m = 1, 2, \ldots, M)$ as shown in Eq. (5) can be obtained. Afterward, the eigenvectors (a vector noted by $\boldsymbol{\beta}_m, m = 1, 2, \ldots, M$) are calculated and used to derive the orthonormal basis $(\boldsymbol{\varphi}_m)$ by projecting the snapshot matrix $\boldsymbol{R}$ on the eigenvectors and then normalize them. Finally, the corresponding coefficients of each POD mode $(c_m^{(k)}, k = 1, 2, \ldots, K, m = 1, 2, \ldots, M)$ are obtained by projecting the snapshot matrix $\boldsymbol{R}$ onto the mode $\boldsymbol{\varphi}_m$. The coefficient contains the magnitude of mth mode $(\boldsymbol{\varphi}_m)$ when reconstructing the kth snapshot $\boldsymbol{s}^{(k)}$ expressed in Eq. (1). Finally, the energy (represented as the kinetic energy of velocity vector field) of all the snapshots captured by mth mode is

$$E_m = \sum_{k=1}^{K} (c_m^{(k)})^2 \tag{6}$$

Identification of Vortex Center and Vortex Core. Vortex structure exists as rotational air motion in the flow field. In this section, simple algorithms are presented to identify the vortex center and vortex core. The vortex center shows the location of the rotational axis, and the vortex core is used to illustrate the vortex strength distribution. Since PIV results show the velocity at discrete spatial locations indicated by discrete arrows in Fig. 5, the images of vortex structure obtained using the algorithms are of the same size as the PIV data, which consists of 25×25 discrete points in this study. To achieve a higher spatial resolution for a better display of the vortex structure, a bilinear filter is used to enlarge the resolution of the vortex identification to the size of the original particle image before the PIV calculation, which is 400×400 pixels.

The vortex center is calculated by finding the location of the maximum absolute value of vorticity. The vorticity described here only relates to the direction of each velocity component. Therefore, the normalization of the velocity field is implemented first, followed by the vorticity calculation. For a given point located at (x, y) in the velocity field, a four-element neighbor is defined as shown in Fig. 4 with the positive sign convention to calculate the vorticity. The variables u and v represent the velocity components in x and y directions, respectively.

Equation (7) gives the formulation of the vorticity at a point (x, y) with known neighbor velocities.

$$\mathrm{Vor}_{(x,y)} = v_{\mathrm{East}} - u_{\mathrm{North}} - v_{\mathrm{West}} + u_{\mathrm{South}} \tag{7}$$

Since the velocity field is normalized to set the velocity magnitude at all points equal to unity, this calculation is similar to the definition used in Ref. [8].

The vortex core is calculated by introducing a convention velocity (denoted by $\overline{\mathrm{CV}}_{(x,y)}$, this term is used in Ref. [8]) at the target location (x, y). It is defined as the four-element neighbor average denoted as $\overline{\mathrm{CV}}_{(x,y)} = (\boldsymbol{w}_{\mathrm{East}} + \boldsymbol{w}_{\mathrm{North}} + \boldsymbol{w}_{\mathrm{West}} + \boldsymbol{w}_{\mathrm{South}})/4$. The velocity vector containing the x and y direction velocities is indicated as $\boldsymbol{w}$. Using the same sign convention shown in Fig. 4, the vortex core is calculated by the formulation shown in Eq. (8). $\tilde{u}$ and $\tilde{v}$ are the velocity components in x and y directions of the velocity vector $(\boldsymbol{w} - \overline{\mathrm{CV}}_{(x,y)})$, which is the original velocity minus the convention velocity.

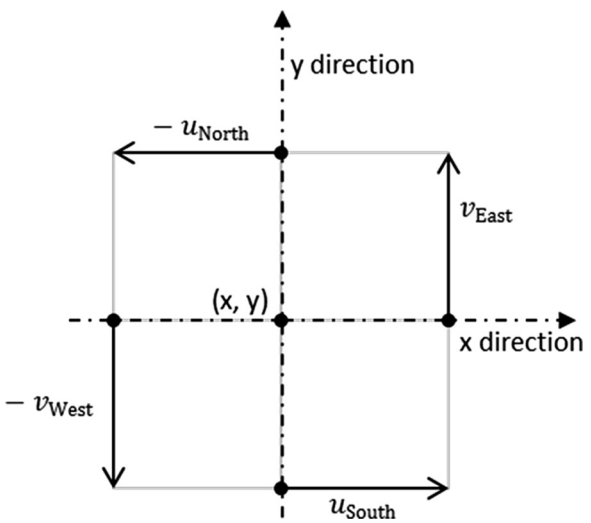

Fig. 4 Four-element neighbor and sign convention for vorticity calculation

$$\mathrm{VorCore}_{(x,y)} = \tilde{v}_{\mathrm{East}} - \tilde{u}_{\mathrm{North}} - \tilde{v}_{\mathrm{West}} + \tilde{u}_{\mathrm{South}} \quad (8)$$

Note that the subtraction of the convention velocity acts as a suppression of macro scale flow motion by leaving the local flow structure alone, so the vortex core calculation can accurately represent the vortex structure distribution.

On the boundary of the velocity field where zero velocity may exist, cautions must be taken to identify the zero velocity points. The neighbor with zero velocity should be eliminated. As a result, the vortex center, convention velocity, and vortex core are calculated with the remaining nonzero velocity points.

Results and Analysis

The cycle-to-cycle variations of the flow fields can be observed at different crank angles from the selected PIV images depicted in Fig. 5. Each row shows a different crank angle degree. Even though the PIV data are collected at every 10 CAD, only the crank angles of −300, −240, −180, −120, and −60 CAD ATDC are used for this paper to illustrate the trends. The first two columns illustrate the images from two individual cycles among the 200 cycles while the last column displays the ensemble average of the 200 PIV images.

It can be found from the flow field images that during the early intake stroke at −300 CAD ATDC, there are strong variations in both velocity magnitude and direction. With the downward motion of piston during the intake stroke, the magnitude of flow velocity at −240 CAD ATDC becomes smaller, but the flow field patterns among the individual cycles and the ensemble flow pattern still show some variations. When the piston reaches the bottom dead center at −180 CAD, the variations are reduced. Finally, no significant differences between individual cycles and the ensemble average of the flow field can be distinguished during the compression stroke.

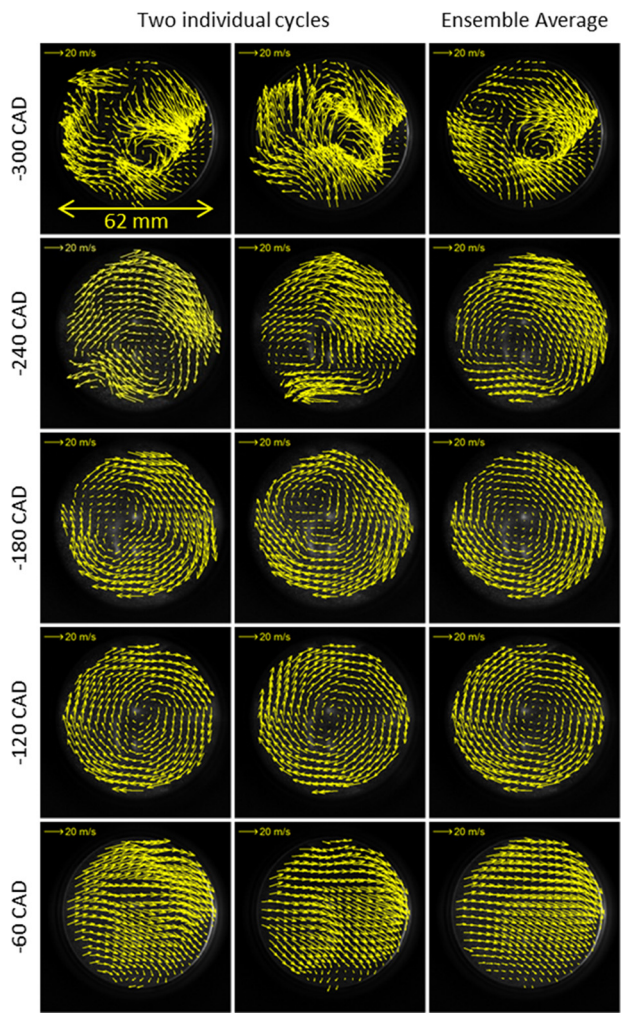

Fig. 5 In-cylinder flow fields of two individual cycles and ensemble average at various crank angles ATDC

Next, the results of vortex center and vortex core are analyzed. The vortex structures of different scales can be found in all the images shown in Fig. 5. Except the images taken during the early intake stroke (−300 CAD ATDC) and late compression stroke (−60 CAD ATDC), all other images show an apparent single dominant vortex structure around the center of the piston. At early intake stroke, there are two effects working together to impact the flow field which leads to the variations of flow field structure, namely (1) the complex intake air charge motion from the intake valves, and (2) the resistance from the piston. While at late compression stroke, the flow field is mainly influenced by the piston movement pushing the vortex structure to the outside of the visible window, so no dominant vortex center can be found in the last row of Fig. 5.

It has been proved by other researchers that the first POD mode possesses the highest energy and the most dominant structure of the snapshots [7,8]. Since large scale vortex structure is the main characteristic of the in-cylinder flow field, the first POD mode can be used to extract this most significant structure and filter out other secondary flow characteristics. Figure 6 shows the first mode of vortex center locations at various crank angles from −300 CAD ATDC to −70 CAD ATDC with 10 CAD time step. The image at −60 CAD ATDC is not shown due to the absence of dominant vortex center. Notice that the vortex center has been squished out of the visible area.

Three different parts of the vortex center motion of the first POD mode can be identified from Fig. 6. The first part is the images from −300 CAD ATDC to −260 CAD ATDC where a multivortex structure of the in-cylinder flow field is found. During this period, the upper right (with respect to the image) intake valve is open while the upper left intake valve is closed, forcing the flow field to move in a clockwise direction. Moreover, as the intake valve opens at this time, an unsteady intake air motion also influences the flow structure. A complex interaction of the intake air with the piston top and the valves interrupts the intake air flow and breaks up the bulk air motion into small-scale vortices. Thus, in addition to the vortex center which is determined by the maximum vorticity, there exist smaller scale vortices with lower vorticity, which are not marked in Fig. 6. During this interval, it is not accurate to obtain flow structure using only one location of the vortex center. This is the reason why the definition of vortex core must be introduced later to provide a more representative description of the flow structure.

The second part starts from −250 CAD ATDC and ends at −100 CAD ATDC which covers the late intake stroke and early compression stroke. During this period, the inertia taken by the intake air has been dissipated by the interaction with air, piston, and cylinder wall. Small-scale vortices are suppressed by the loss of the original kinetic energy of the intake air. Furthermore, the piston moves to the location far away from the focal plane, and it reduces the disturbance from the piston top to the flow field structure. Hence, the flow fields in the second part exhibit similar single vortex structure with the vortex center locating around the center of the piston.

At the later compression stroke from −90 CAD ATDC to −60 CAD ATDC, the third part of the vortex center motion can be observed. During this period, the piston is moving upward toward the focal plane. It pushes the flow structure to the edge of the visible area and the vortex finally disappears. The geometry of the piston top contributes to this process. Since the piston used in this study is a flat piston, the flow structure is kept similar to the flow in second part. The slightly asymmetric shape of the piston

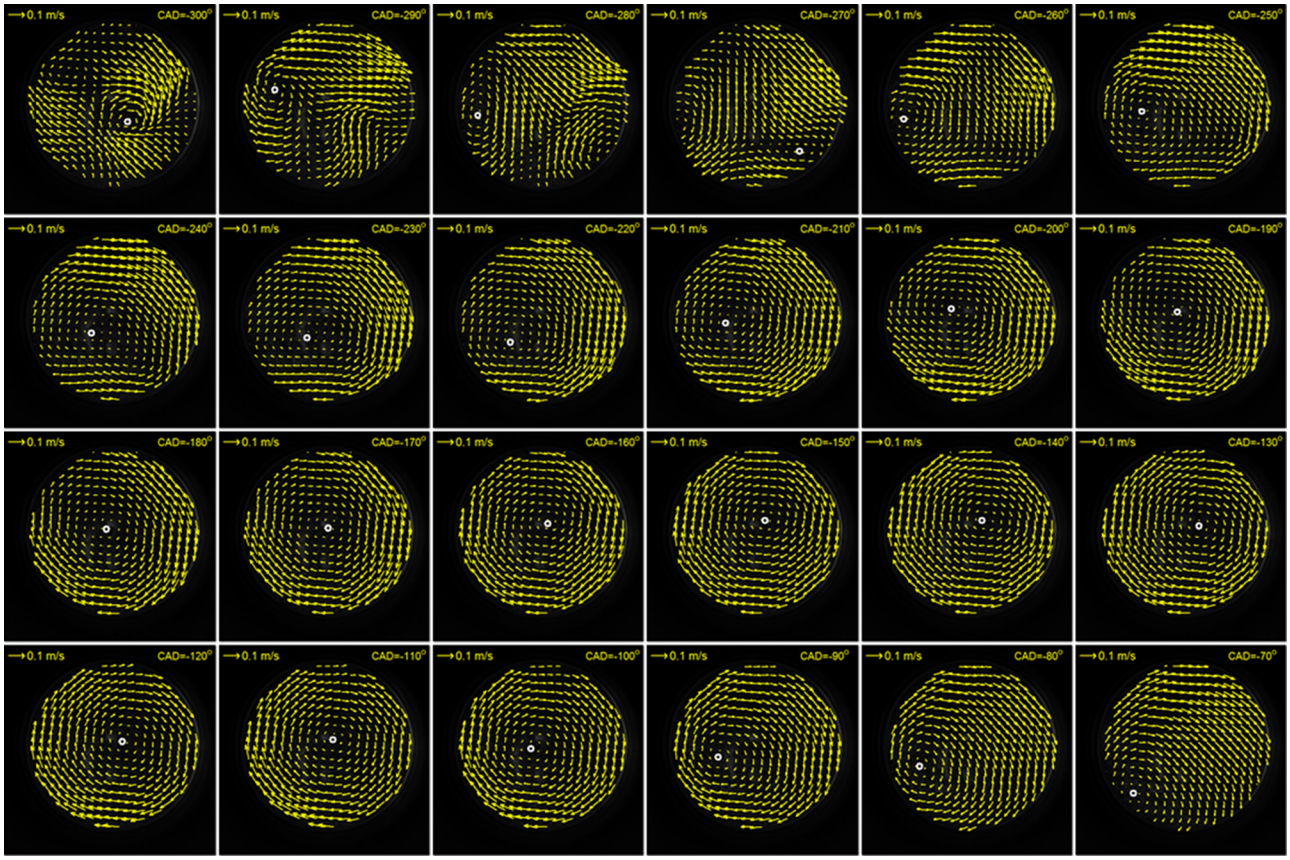

Fig. 6 Vortex center location (white circle) evolution of POD mode 1 from −300 CAD ATDC to −70 CAD ATDC. (The vortex center is out of visible area at −60 CAD ATDC.)

and cylinder head leads to the result that the vortex center finally moves to the left bottom direction in the image.

In addition to the first mode of capturing the main characteristics of single vortex structure, the higher POD modes represent the fluctuating structures of the flow field. Applying the vortex core identification algorithm to the higher modes improves the understanding of variations of the vortex structure at various crank angles. The vortex core structures of the first three POD modes at crank angles from −300 CAD ATDC to −60 CAD ATDC with 60 CAD step are depicted in Fig. 7. The first column shows the first POD mode which is the same dataset used in Fig. 6 for identifying the vortex center. At the intake stroke, there are a few vortices with different directions and length scales. A main vortex in clockwise direction can be observed in the first POD mode due to the intake swirl motion. At the boundary, there exist some small vortices in the opposite direction. The strong interactions of the intake air are consistent with the conclusion by analyzing the PIV images.

The vortex core becomes uniform in later crank angles until the end of compression stroke. During this process, the piston is moving away from the focal plane, causing limited influence on the air motion along this plane. The flow field can retain its original structure and energy. Moreover, the energy captured by the first mode of these three crank angles is more than 90% among total 200 modes. This means that only very small variations appear during this process.

The vortex core strength at −60 CAD ATDC shown in the last column in Fig. 7 is clearly smaller than the strength at early compression stroke. This phenomenon is caused by the absence of vortex structure in the visible area. The piston pushes the vortex center out of the visible area, which makes the flow field in the cylinder become a directional structure without a strong vortex. The geometry of combustion chamber and asymmetric pent-roof determines the direction to which the air is squished. This will only happen if the piston top is flat. For other bowl shape pistons, the air will be disturbed much more strongly at the end of compression stroke. The second and third modes of the vortex core illustrate the most significant variations of the vortex structure at various crank angles shown in Fig. 7. Smaller scale vortices can be found in both mode 2 and mode 3 at different locations and with different directions. Although the second and third modes in different crank angles show very strong multivortex structures, the total energy captured by those two modes are very limited as indicated in Fig. 8.

However, from the energy fraction shown in Fig. 8, it can be observed that strong variation exists during the intake stroke at −300 CAD ATDC. The energy fraction indicates that less energy is captured by the first mode comparing to other crank angles, which means that the higher modes contain more energy of the flow field. Moreover, the spatial variations of the vortex core can also be found at −300 CAD (first row) in Fig. 7. Therefore, the flow during the period near −300 CAD ATDC has stronger variations than the crank angles at late intake stroke and compression stroke.

With the motoring of the engine, the energy fraction captured by the first mode increases to around 90% in the later intake stroke and early compression stroke (−240, −180, and −120 CAD ATDC). The flow structure of first mode shows a uniform vortex core distribution while the higher modes still exhibit multiple vortices. However, the energy captured by higher modes has been suppressed due to the lack of air interaction with each other and with the piston top.

Recall that the PIV image at −60 CAD ATDC shows a regular flow structure without vortex center in the visible area, thus the

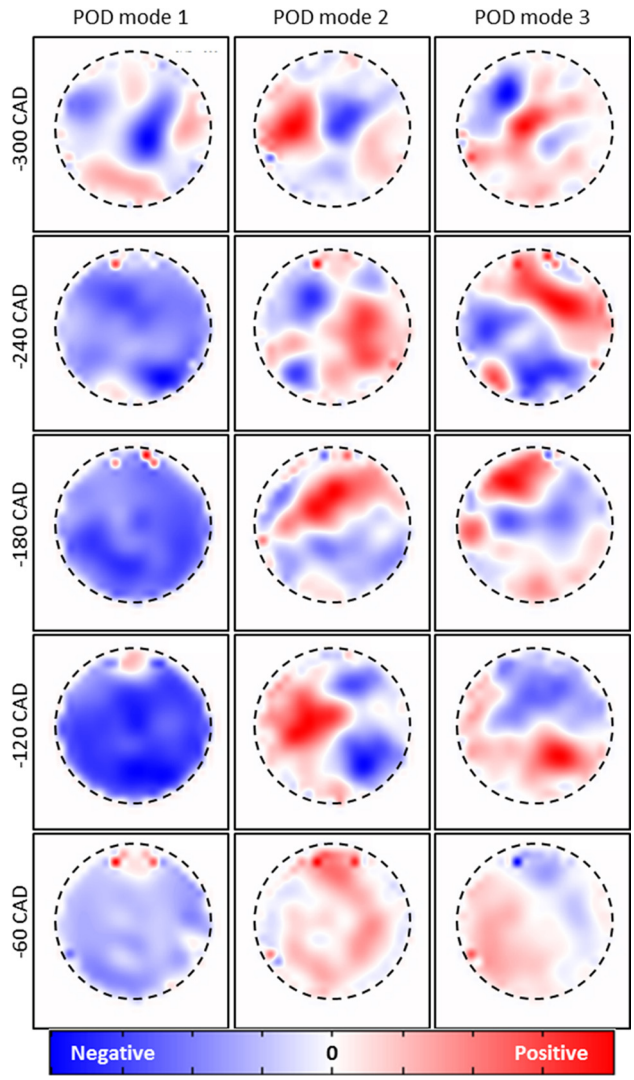

Fig. 7 Vortex core structures of first three POD modes at various crank angles. Dashed circle indicates the visible area of the optical piston. The unexpected dots at the edge are due to the noise from the image processing.

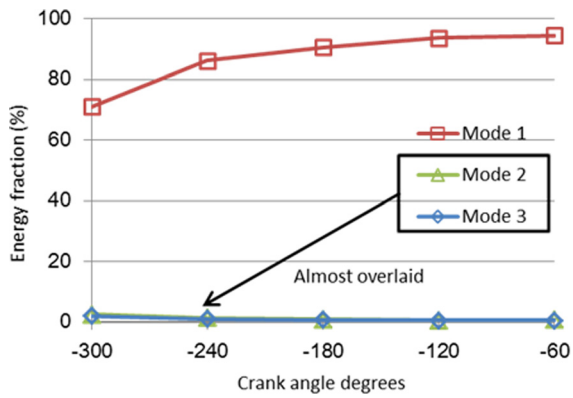

Fig. 8 Energy fraction captured by first three POD modes at different crank angles

flow in the image looks like a directional flow without vortex. That is the reason why no strong vortex structures are shown in the first mode. At the same time, the less disturbed higher modes indicate that very small variations are taking place at this crank angle.

Summary

In this study, high-speed PIV experiments were implemented to study the time-resolved in-cylinder flow fields. 200 consecutive cycles of images were recorded from −300 CAD ATDC to −60 CAD ATDC with a time step of every 10 CAD. Simple algorithms were developed to identify the vortex center and vortex core from the PIV data. Experimental PIV data show that multivortex structures exist during the early intake stroke, and they evolve into a single vortex structure during the compression stroke. The flow structure with multiple vortices in the intake stroke is likely caused by the complex intake flow motion interactions between the intake air and the valves, piston and cylinder wall. However, after the kinetic energy of the intake air has been dissipated, the in-cylinder flow forms a single vortex structure starting from the bottom dead center until the end of compression stroke. Tracking the vortex center at different cycles shows that the vortex center moves to random locations during the intake stroke while the vortex center stays much closer to the middle of the piston during the compression stroke. POD was then applied to analyze the variations of flow fields. Applying the POD to the same set of PIV data has resulted in a set of orthonormal modes which capture the variation characteristics of the original PIV flow fields. The first POD mode shows the most dominant flow fields which are similar to the ensemble PIV data. The higher modes capture the smaller structural variations of the flow field. Moreover, the second and third modes mostly capture the main variations which show multivortex structures at all crank angles.

The technique demonstrated in this paper provides a better understanding of the time-resolved variations of vortex structure in the flow field of a SIDI engine. The POD analysis method is able to separate the variations of the dominant flow structure from the small-scale flow fluctuations. Meanwhile, the developed vortex analysis algorithms both clarify the in-cylinder flow characteristics by tracking the vortex center motion and illustrate the cycle-to-cycle variations of the flow field as indicated by the vortex core. Further development of the study will be implemented to quantitatively resolve the strength of vortex core and extend the analysis technique to different intake swirl ratios and engine speeds.

Acknowledgment

This research is sponsored by the General Motors Company (USA) and National Natural Science Foundation of China (NSFC) under Grant No. 51176115. This was carried out at the National Engineering Laboratory for Automotive Electronic Control Technology of Shanghai Jiao Tong University. The funding was provided by the National Natural Science Foundation of China (NSFC) under Grants Nos. 51076093/E060702 and 51176115/E060404, SJTU Engineering-Science Interdisciplinary Research Fund, and 2009 Program for New Century Excellent Talents in University by China Ministry of Education (MOE).

Nomenclature

ATDC = after top dead center
CAD = crank angle degree
PIV = particle image velocimetry
PLIF = planar laser induced fluorescence
PM = particulate matter
POD = proper orthogonal decomposition
SIDI = spark-ignition direct-injection

References

[1] Sick, V., 2013, "High Speed Imaging in Fundamental and Applied Combustion Research," Proc. Combust. Inst., **34**(2), pp. 3509–3530.
[2] Sick, V., Drake, M. C., and Fansler, T. D., 2010, "High-Speed Imaging for Direct-Injection Gasoline Engine Research and Development," Exp. Fluids, **49**(4), pp. 937–947.

[3] Ho, S.-S., 2012, "An Effective Vortex Detection Approach for Velocity Vector Field," 21st International Conference on Pattern Recognition (ICPR2012), Tsukuba, Japan, Nov. 11–15, pp. 2643–2646.
[4] Li, Y., Zhao, H., Peng, Z., and Ladommatos, N., 2001, "Analysis of Tumble and Swirl Motions in a Four-Valve SI Engine," SAE Trans. J. Engines, **110**, pp. 2226–2241.
[5] Müller, S., Böhm, B., Gleißner, M., Grzeszik, R., Arndt, S., and Dreizler, A., 2010, "Flow Field Measurements in an Optically Accessible, Direct-Injection Spray-Guided Internal Combustion Engine Using High-Speed PIV," Exp. Fluids, **48**(2), pp. 281–290.
[6] Chen, H., Reuss, D. L., and Sick, V., 2011, "Analysis of Misfires in a Direct Injection Engine Using Proper Orthogonal Decomposition," Exp. Fluids, **51**(4), pp. 1139–1151.
[7] Chen, H., Reuss, D. L., and Sick, V., 2012, "On the Use and Interpretation of Proper Orthogonal Decomposition of In-Cylinder Engine Flows," Meas. Sci. Technol., **23**(8), p. 085302.
[8] Graftieaux, L., Michard, M., and Grosjean, N., 2001, "Combining PIV, POD and Vortex Identification Algorithms for the Study of Unsteady Turbulent Swirling Flows," Meas. Sci. Technol., **12**(9), pp. 1422–1429.
[9] Cosadia, I., Borée, J., and Dumont, P., 2007, "Coupling Time-Resolved PIV Flow-Fields and Phase-Invariant Proper Orthogonal Decomposition for the Description of the Parameters Space in a Transparent Diesel Engine," Exp. Fluids, **43**(2–3), pp. 357–370.
[10] Chen, H., Reuss, D. L., Hung, D. L., and Sick, V., 2012, "A Practical Guide for Using Proper Orthogonal Decomposition in Engine Research," Int. J. Engine Res., **14**(4), pp. 307–319.